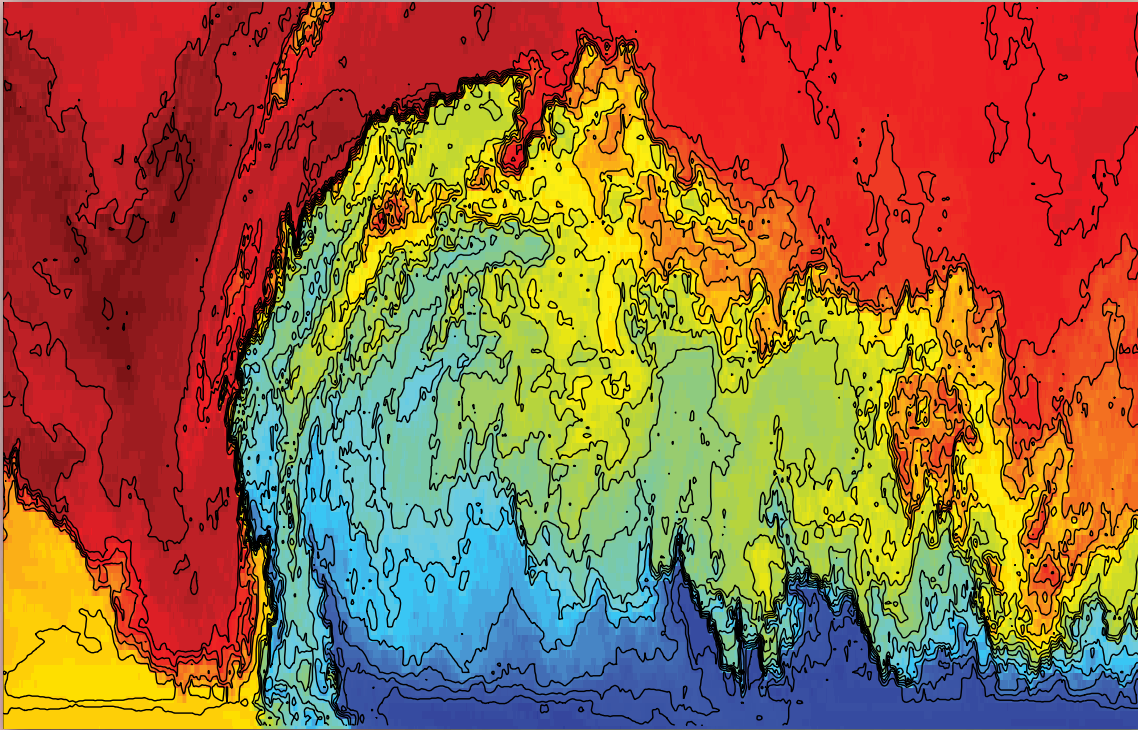


Energy Release Through Internal Wave Breaking

BY HANS VAN HAREN AND LOUIS GOSTIAUX



ABSTRACT. The sun inputs huge amounts of heat to the ocean, heat that would stay near the ocean's surface if it were not mechanically mixed into the deep. Warm water is less dense than cold water, so that heated surface waters "float" on top of the cold deep waters. Only active mechanical turbulent mixing can pump the heat downward. Such mixing requires remarkably little energy, about one-thousandth of the heat stored, but it is crucial for ocean life and for nutrient and sediment transport. Several mechanisms for ocean mixing have been studied in the past. The dominant mixing mechanism seems to be breaking of internal waves above underwater topography. Here, we quantify the details of how internal waves transition to strong turbulent mixing by using high-sampling-rate temperature sensors. The sensors were moored above the sloping bottom of a large guyot (flat-topped submarine volcano) in the Canary Basin, North Atlantic Ocean. Over a tidal period, most mixing occurs in two periods of less than half an hour each. This "boundary mixing" dominates sediment resuspension and is 100 times more turbulent than open ocean mixing. Extrapolating, the mixing may be sufficiently effective to maintain the ocean's density stratification.

ABOVE | A large backward-breaking internal wave is depicted in this time-depth image whose axes are 14 minutes horizontally and 50 m vertically. This wave was observed using 101 high-sampling-rate temperature sensors between 0.5 and 50 m above the bottom at 550 m depth near the top of Great Meteor Seamount, North Atlantic Ocean. Temperature ranges from 12.3°C (blue) to 14.1°C (red); contour intervals are every 0.1°C (black).

INTRODUCTION

Internal waves are ubiquitous around the globe in estuaries, seas, and oceans, causing their interiors to be in constant motion. They exist because these waters all have stable density stratification from surface to bottom. Ocean water density is mainly determined by temperature and salinity variations (Box 1). Vertical density differences (“stratification”) create a restoring force for wave motions in the interior (“internal waves”). High-resolution temperature measurements show the omnipresence of internal waves near beaches and at great depths, with similar features persisting at a wide variety of scales, thus resembling a fractal world (Figure 1; note the 100–1,000 times different depth-time ranges and the factor of 1,000 smaller temperature range in panel d). Such features include overturning of occasionally large 50 m high fronts (image on opposite page) followed by a trail of turbulent high-frequency internal waves. The ocean interior’s 10–100 m high weakly turbulent internal waves can thus mix and transport material when

they reach strong turbulence states above underwater topography (Thorpe, 1987a). The turbulence is visible as closed loops of a wide range of sizes. These loops can transport material and affect stratification. Quantification of such mixing processes thus requires detailed observations using a high sampling rate (once per second) and precise instrumentation.

There are two dominant internal wave sources near the lowest internal wave frequency: “inertial” motions, which result from an adjustment to large-scale disturbances such as fronts or atmospheric storms in combination with Earth’s rotation, and internal tides, which result from the interaction of surface or “barotropic” tidal motions with topography. Whereas inertial motions can be observed dominantly near the ocean’s surface or in closed seas like the Mediterranean (Figure 1d), internal tides are dominant in the open ocean (Figure 1a). Compared to surface waves that are generated through the much larger density difference between air and water, internal waves travel slowly because the lower

density contrast between different water layers generates weaker restoring forces. These internal waves have periods varying from one day, depending on Earth’s rotation, down to several minutes, depending on stratification.

Low-frequency, long-period near-inertial internal wave motions have relatively small vertical wave lengths of 10–100 m in the open ocean (1–10 m in shallow seas). These small length scales cause the inertial currents to vary rapidly in the vertical, creating large vertical current differences (termed shear or internal friction). The resulting shear-induced turbulent mixing occurs infrequently in the open ocean, creating about one-quarter to one-third (Gregg, 1989) of the global, ocean-wide vertical turbulent diffusivity (a measure for vertical exchange with units of $K_z = 10^{-4} \text{ m}^2 \text{ s}^{-1}$; Munk, 1966) needed to maintain deep-ocean (heat) stratification. Hence, another energy sink should exist, and much additional energy is lost near underwater topography such as seamounts and continental slopes.

BOX 1 | TEMPERATURE AS A TRACER FOR DENSITY VARIATIONS

The dynamics of vertically varying ocean motions depend on variations in density. Though ocean density variations cannot be measured directly, density is mainly (more than 99.99%) determined by variations in temperature, salinity, and pressure. A vertically stable water column is composed of warm, fresh water over cold, salty water. Warmer water is less dense than colder water when salinity is 23 or more parts per thousand (ppt). An average ocean value is 35 ppt. Freshwater is less dense than salty water. Roughly 4°C in temperature and 1 ppt in salinity each contribute to $\pm 1 \text{ kg m}^{-3}$ in density variations. Although the static pressure increases by 1 bar (atmosphere) every 10 m vertically in the ocean, it is the small (1%) compressibility of water that affects density variations.

In terms of observational techniques, temperature and pressure

are the easiest to observe. Salinity is measured indirectly, using a combination of temperature and conductivity sensors. Temperature observations alone can be used at a particular known pressure (depth) as a replacement (proxy) for density variations, provided the density-temperature relationship is well known (tight). This relationship can be established by repeatedly lowering a shipborne conductivity-temperature-pressure package at the site of interest.

If the vertical density variations are very small, about 0.001 kg m^{-3} per 100 m, high-precision sensors can observe temperature to increase with pressure (depth) while density remains stable. The limit of this increase is the adiabatic lapse rate of about $1.7 \times 10^{-4} \text{ }^\circ\text{C m}^{-1}$, which is due to the compressibility of water. It can be easily corrected for when pressure (depth) is known.

Because the interaction of horizontal motion with sloping underwater topography generates internal tides (part of the low-frequency internal waves), it is conjectured that most mixing also occurs along the ocean's sloping boundaries rather than in its interior (Munk, 1966; Armi, 1978; Thorpe, 1987b; Garrett, 1990, 1991). The concentration of internal tidal energy may cause enhanced wave breaking and mixing. Internal waves constitute a partial (20%) sink for tidal energy, or about 0.6 TW globally (Munk and Wunsch, 1998). If the boundary mixing described is efficient enough, it should account for mean energy loss (dissipation) of 1.5 mW m^{-2} .

However, it is unclear how energy transfers from the internal wave source to its turbulence loss, but it is probably via small-scale internal waves.

At the high-frequency end of the internal wave spectrum, short-period waves near buoyancy frequency N are the natural motions following stratification disturbance (Groen, 1948). N^2 is proportional to the vertical density stratification and the acceleration of gravity. These waves are close to turbulence in frequency (D'Asaro and Lien, 2000). One possible explanation for how high-frequency internal waves transition to turbulence is through interaction with near-inertial or tidal shear, which

deforms the internal waves and makes them overturn. Another possible explanation is that high-frequency internal waves deform to linear or nonlinear internal tides and then disintegrate into high-frequency solitary waves (Gerkema, 1996; Farmer et al., 2011). Despite their name, such high-frequency nonlinear waves generally do not occur alone, but instead commonly occur in groups of four to ten waves (Helfrich and Melville, 2006). When such solitary wave groups, carried by the internal tidal wave, collide with underwater topography, they transform (Orr and Mignerey, 2003), and the leading one sharpens into an upslope frontal bore (Vlasenko and Hutter, 2002; Klymak and Moum, 2003). Such a bore dominates sediment resuspension (Hosegood et al., 2004; Bonnin et al., 2006), which resembles an atmospheric dust storm.

Here, we present detailed observations demonstrating that internal wave motions above sloping topography are indeed quite different from those in the ocean's interior. High-resolution moored temperature sensors (Box 2) offer the best way to study the process of internal wave-turbulence dynamics. The sensors must be used in areas where temperature has a known relationship with density variations. The moored sensors are used to quantify several turbulence parameters, following a method established from shipborne conductivity-temperature-depth (CTD) and microstructure profiler data.

OBSERVATIONS FROM THE OCEAN INTERIOR

The stratified interiors of the open ocean and shallow seas are permanently in motion between surface and bottom, with typical ocean amplitudes reaching several tens of meters. This stratification

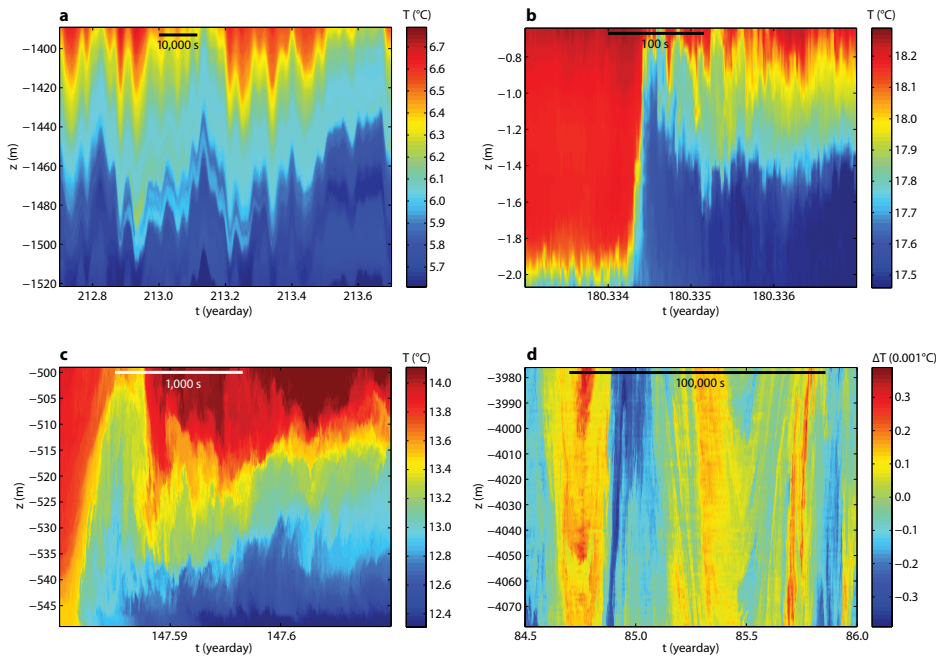
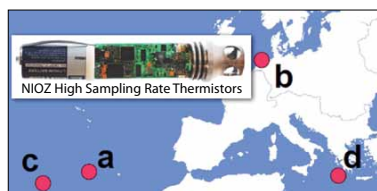


Figure 1. Examples of time-depth internal wave-turbulence temperature observations obtained in widely varying ocean environments (see lower left panel) using moored NIOZ-HST high-sampling-rate temperature sensors. (a) One-day section showing smooth tidal and higher-frequency internal waves with 130 m amplitude, from the Canary Basin, Northeast



Atlantic Ocean (van Haren and Gostiaux, 2009). (b) Six-minute section showing a 1.75 m high front and turbulent wave motions, using data gathered from instruments on a pole at Texel beach in the Netherlands (van Haren et al., 2012). (c) A 2,500 second section showing a 50 m high breaking wave and trailing high-frequency internal waves and turbulence above a slope of Great Meteor Seamount, Northeast Atlantic Ocean (van Haren, 2005; van Haren and Gostiaux, 2012). (d) A 1.5 day section in the Ionian Sea, eastern Mediterranean, showing 100 m high inertial waves (period = 20.06 hrs) and turbulent overturning observed relative to the adiabatic lapse rate (Box 1), thereby reaching the limits of the high-precision sensors (van Haren and Gostiaux, 2011).

is visible in a one-day example composite of 54 NIOZ (Royal Netherlands Institute for Sea Research) temperature sensors that sampled stratification around 1,450 m at 33°00.010'N, 22°04.841'W (5,274 m water depth) in the Canary Basin, Northeast Atlantic Ocean (Figure 1a). Although these particular open-ocean observations are less than ideal because of the influence of warm, salty Mediterranean outflow waters between 1,000 and 1,500 m depth that regularly appear as apparent inversion layers, the observations are useful for studying internal wave motion variability. The motions are smooth, although not perfectly sinusoidal in shape, and have relatively large vertical coherent scales with near-zero phase difference over the 130 m range of temperature sensors at both tidal and near-buoyancy frequencies. Peak-to-trough wave heights are several tens of meters.

These motions are found throughout the 1.5-year record, but amplitudes vary continuously per frequency band. The stratification is also subject to substantial variation. The thickness of strongly stratified layers drops below sensor separation, in this case 2.5 m, while the thickness of weakly stratified layers can exceed 50 m. Overturns are few and far apart despite the 1 Hz sampling, but due to the ill-defined density-temperature relation in these variable water masses under intermediate Mediterranean Sea influence, quantification of turbulence parameters (Box 2) is difficult. In addition, a small portion of the larger overturn scales is resolved by the 2.5 m vertical sensor separation, as compared to the mean Ozmidov scale $L_O = 0.5$ m. This scale represents the largest vertical turbulence scales under stratified conditions. Turbulence parameter estimates are made, in this case, using

limited conventional CTD measurements at stations nearby, which provide typical values of $K_z = 2-3 \times 10^{-5} \text{ m}^2 \text{ s}^{-1}$ and $\varepsilon = 10^{-9} \text{ W kg}^{-1}$ over the range of the temperature sensors. These values are in the same range as previously estimated from upper (< 2,000 m) open-ocean microstructure observations (e.g., Gregg, 1989).

WHEN A WAVE MEETS A SEAMOUNT

Near a large guyot like Great Meteor Seamount, an internal tidal wave moves warm water down during one tidal phase

Hans van Haren (*hans.van.haren@nioz.nl*) is Senior Scientist, NIOZ Royal Netherlands Institute for Sea Research, Den Burg, the Netherlands. **Louis Gostiaux** is CNRS Scientist, INP/UJF-Grenoble 1, Laboratoire des Ecoulements Géophysiques et Industriels, Grenoble, France.

BOX 2 | MIXING MEASUREMENTS USING MOORED SENSORS

Modern electronics allow the manufacture of once per second (1 Hz) high-sampling-rate temperature sensors (HST) at NIOZ. These NIOZ-HST offer precision better than 0.001°C and a very low noise level of $6 \times 10^{-5} \text{ }^\circ\text{C}$. They can be used down to 6,000 m and have the potential of one-year uninterrupted stand-alone operation running on a single small battery (van Haren et al., 2009). They have been developed specifically for use in a vertical array of many sensors (about 100) to study dynamic processes such as fronts and internal waves in shallow seas and the deep ocean. A key element is their synchronization in time, which is enforced through electromagnetic induction. At a preset interval of less than a day, all clocks are synchronized to a single standard. The clock synchronization is better than 0.1 s, permanently during deployments of up to two years. Under conditions of sufficient vertical spatial resolution and of temperature acting as a proper tracer for density variations, these moored sensors are excellent for quantifying turbulent mixing in great detail that is generated by the dynamic processes described above (van Haren and Gostiaux, 2012).

Turbulence makes a vertically stable water column locally unstable by overturning denser (colder) water above less-dense

(warmer) water during brief moments. This phenomenon is clearly observed when a large breaking wave passes the sensors (see figure on page 126). Quantification of mixing is done by re-enacting the turbulence of each 1 Hz vertical temperature profile: all unstable portions are computationally sorted (reordered) to their stably stratified positions in a monotonic profile without overturns (Thorpe, 1977). The reordering vertical displacements (d) are a measure of the turbulence following empirical relations, which have a constant mixing efficiency of 0.2 (Osborn, 1980) and $d = 1.25 L_O$ (Dillon, 1982). L_O represents the Ozmidov scale for large overturns in stratified fluids. The constant values still seem to hold today, specifically for the ocean, which is nearly always turbulent. The Reynolds numbers are high, between one thousand and one million. Such values are especially found above sloping topography, where ocean turbulence can be very high, but stratification is also constantly restored, mainly in thin layers (van Haren, 2005). When stratification is restored, mixing is efficient. This efficient mixing, estimated from the larger, energetic turbulent overturns, is expressed in its main parameters' turbulent exchange rate or diffusivity K_z and turbulence energy loss or dissipation rate ε .

and cold water up along the sloping bottom during the next phase (Figure 2a). These observations are made using 101 temperature sensors spaced every 0.5 m between 0.5 and 50 m above the bottom at 30°00.052'N, 28°18.802'W in 549 m water depth. This depth is about 200 m below the summit of the 4,000 m high guyot. The local bottom slope is supercritical for internal tides (van Haren and Gostiaux, 2012). Here, in contrast to rather smooth open-ocean tidal fluctuations, the tidal fluctuations become rugged and steep above sloping topography. This translates into a quasi-permanent state of turbulent overturning in the lower 50 m above a seamount's slope. This turbulence varies by nearly four orders of magnitude (Figure 2b). Smaller turbulence peaks are associated with 5 to 10 m high overturns of 30 to 300 s duration some distance off the bottom (van Haren and Gostiaux, 2010). Largest peaks are associated with big overturns during the upslope phase (van Haren and Gostiaux, 2012). They

can reach dissipation rate values of 1 W m^{-2} integrated over the 50 m range of observations during a few minutes.

Viewed in more detail, Figure 3 shows the vigorous turbulence of a large overturning internal tidal wave. The sudden change from a warming to a cooling tidal phase is associated with an upslope-moving frontal bore that occurs once or twice every tidal period. When we compare the raw data (Figure 3a) with the stably stratified reordered data (Figure 3b; see Box 2 for method), we see that part of the turbulence is associated with the large backward-breaking wave. The raw data provide an image with lighting that appears three-dimensional (like seventeenth-century Dutch paintings), while the image of reordered data has a flat two-dimensional appearance. The reordering clearly straightens the large front that was originally curved.

Within a meter of the seafloor, the reordered stable stratification (Figure 3c) appears very thin (down to the lowest vertical resolution of 0.5 m) just prior

to the passage of the front. Reordering displacements (Figure 3d) delineates the turbulent patches or overturns, as well as overturns within overturns, down to about the scale of vertical resolution. Typical patches have sizes of 10 m in the vertical and 300 s in time, but smaller and also larger ones occur, even exceeding the 50 m range of sensors (e.g., around day 146.57). The average 20 m L_O is well resolved by the 0.5 m distance between sensors.

Such large displacements result in local turbulent diffusivity up to $K_z = 0.1\text{--}1 \text{ m}^2 \text{ s}^{-1}$ (Figure 3e). Large K_z values are generally estimated within layers of less-stable stratification, with the exception of high values in thin, strongly stratified layers such as those forcing a big front or nonlinear bore. The front stands out more clearly in the dissipation rate image, extending along its entire length $\varepsilon = 10^{-5}\text{--}10^{-4} \text{ W kg}^{-1}$ in Figure 3f. In this image, it is clear that the front is the only turbulent overturn extending from the bottom upward, which is important for sediment resuspension. All other larger and smaller overturns are located within the turbulent water column away from the bottom.

Tidal up- and down-slope motion powers the general pattern of the turbulence dissipation rate, but, in part, the shortest freely propagating internal waves near the buoyancy frequency power smaller-scale turbulent patches. In the hour around the frontal bore (roughly the period of Figures 3 and 4), we observe high-frequency internal waves near the local thin-layer buoyancy frequency up to $N = 0.01 \text{ s}^{-1}$, resulting in buoyancy periods just over 10 minutes. These motions become more intense and of shorter duration just prior to arrival of the front, thereby depressing the stratification to within a few meters of the

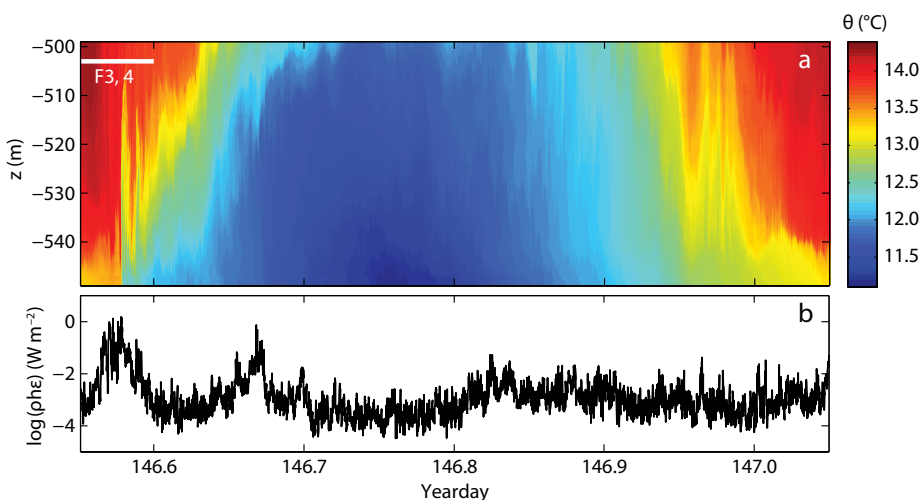


Figure 2. One tidal period of temperature observations using 101 temperature sensors above Great Meteor Seamount, sampled at 1 Hz. (a). The time-depth image shows a tidal wave well beyond the 50 m range of the sensors. Smaller/shorter-scale waves are also visible. The white bar indicates the period of Figures 3 and 4. (b). Time series of turbulence dissipation rate ε , inferred from the data in (a), times density ρ and integrated over the vertical range of the sensors, $h = 50 \text{ m}$ (log scale). Most turbulence occurs in brief periods of fewer than 10 minutes during the upslope (cooling) phase of the tide.

bottom. After the steep frontal passage, the apparent wave period is elongated, at about the same pace as turbulent mixing reduces stratification, and it is shortened again upon restratification (day 146.95–146.97 in Figure 2).

ASSOCIATED CURRENTS

Typical internal-tide-generating, large-scale barotropic horizontal currents flow at 0.1 m s^{-1} over the top of the seamount (Mohn and Beckmann, 2002; confirmed by TXPO Topex Poseidon satellite data on surface elevation) and only 0.02 m s^{-1} in the ocean interior (Gerkema and van Haren, 2007). Nash et al. (2007) observed similar, relatively small internal-tide-generating currents over the Oregon continental slope. Nevertheless, these weak currents can have spectacular impacts when they produce internal waves breaking in the near interior. As Figure 4 shows, large overturns away from the bottom just prior to arrival of the frontal bore are associated with relatively large downward motions originating from above the sensors (the negative/blue vertical current). This downdraft is caused by intensification of the high-frequency internal waves around the turbulent bore. The front is sharpened when interior overturns that precede the bore are large and intense. During the three-minute passage of the bore, cross-slope current changes from 0.2 m s^{-1} downslope to 0.4 m s^{-1} upslope (Figure 4c), and the along-slope current changes sign (Figure 4d). Upward vertical currents reach $w = 0.15 \text{ m s}^{-1}$ (Figure 4b), and the front dominates sediment resuspension, moving sediment more than 50 m up from the bottom. This sediment resuspension is inferred from sediment trap and acoustic backscatter data (Hosegood et al., 2004). Here, such sediment resuspension

related backscatter increases by a factor of 1,000 (Figure 4a).

The large vertical internal wave currents, occurring more or less every tidal period, may in turn generate internal tidal waves that are modulated by the 10% variation in time of arrival of the frontal bore (van Haren, 2006). In spite of their short duration of only $T_w/2 = 3 \text{ mins}$ (half period), they compete for internal tide generation with the large-scale (barotropic) vertical current W_{SD} over semidiurnal tidal period T_{SD} , which is commonly used in internal tide models. Averaged over a tidal period, $w \times T_w/T_{SD} = 0.0012 \text{ m s}^{-1}$, which is comparable with $W_{SD} = 0.002 \text{ m s}^{-1}$

used for conversion in the vicinity of Great Meteor Seamount (Gerkema and van Haren, 2007).

DISCUSSION

Integrated over the 50 m range of the sensors, the three-minute frontal passage dissipates an average of 1.5 W m^{-2} , equivalent to peak values observed in the South China Sea, where one of the world's largest internal tides occurs (St. Laurent et al., 2011). When establishing a cumulative sum of energy dissipation over the Figure 2 tidal period, this three-minute frontal “sediment resuspension power” contributes 21% to the average energy dissipation rate of

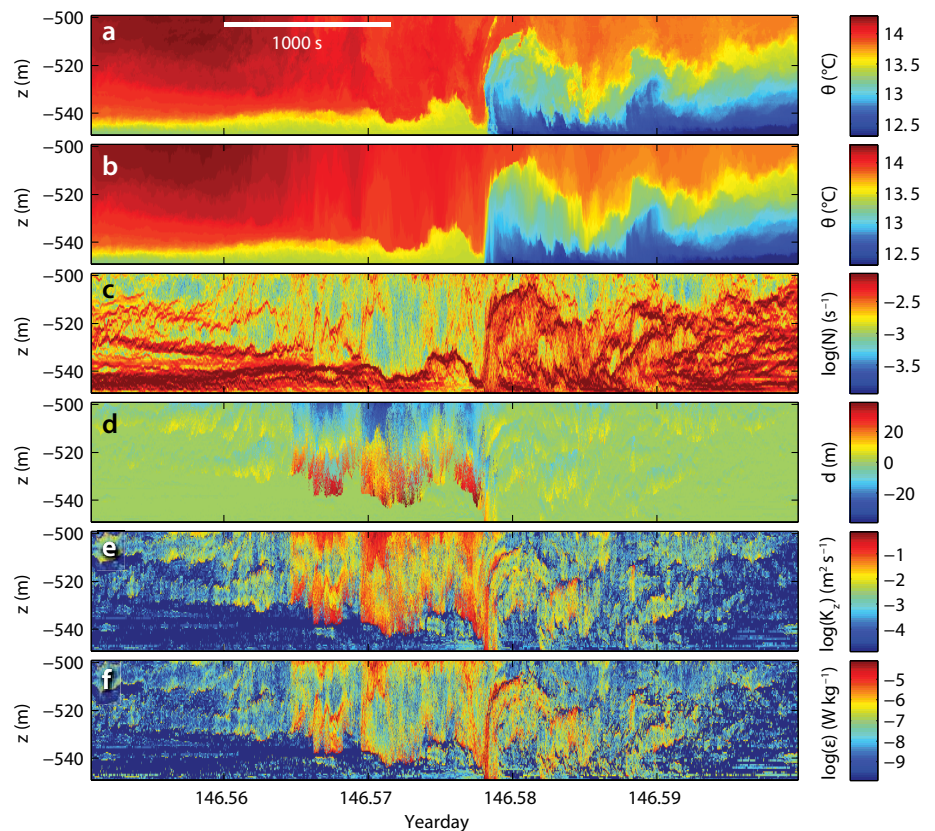


Figure 3. Time-depth images of temperature and quantified turbulence during the 4,500 s period indicated at upper left in Figure 2a prior to and into an upslope moving, cooling tidal phase. (a) Potential temperature after pressure-corrected calibration. (b) Reordered potential temperature profiles every 1 Hz time step (see Box 2 for method). (c) Stable density stratification computed from (b) using a tight temperature-density relationship from CTD observations near the mooring. (d) Reordering displacements following comparison of (a) and (b). (e) Turbulent diffusivity. (f) Turbulence dissipation rate. In (e) and (f), dark blue also indicates below threshold (after van Haren and Gostiaux, 2012).

9.5 mW m⁻². About 65% of this average occurs in the 75 minutes shown in Figures 3 and 4, and another 10% occurs during the 10-minute collapse of a second front around day 146.67 (Figure 2). Like the main frontal bore, this second-front turbulence also reaches the bottom, but from above. Similar values are found in every tidal period over the 18-day record (van Haren and Gostiaux, 2012).

Eighteen days of observations yielded the mean $[K_z] = 0.003 \pm 0.001 \text{ m}^2 \text{ s}^{-1}$ and the mean $[\epsilon] = 1.5 \pm 0.7 \times 10^{-7} \text{ W kg}^{-1}$, which give 7.5 mW m⁻² for the 50 m vertical range of observations. These values are comparable to values from (micro-structure) profiler data over the Hawaiian Ridge (Aucan et al., 2006; Klymak et al., 2006) and above the Oregon continental slope (Nash et al., 2007). The average dissipation rate is set by nonlinear wave breaking rather than by bottom friction. When extrapolated to the entire area around Great Meteor Seamount (about 100 × 100 km²), the tidally averaged

dissipation rate is 75 MW. This figure is one-quarter of the estimated conversion into internal tidal energy by Great Meteor Seamount (Gerkema and van Haren, 2007). We note that the present dissipation rate estimate is for the 50 m vertical range of sensor observations, but because at least 30% of the high/low values are found right near the upper edge of observations (Figure 3d,e around day 146.57), we estimate our values to be higher. A rough estimate would be about a factor of two larger, or a turbulent boundary layer of 100 m.

If we hypothetically extrapolate further and use previous estimates (Armi, 1978, 1979; Garrett, 1990, 1991) that about 3% of the ocean is occupied by 100 m high turbulent boundary layers above sloping topography, we find a mean ocean-basin interior K_z of 10⁻⁴ m² s⁻¹, which is the value needed to maintain the overall density stratification (Munk and Wunsch, 1998). This value supports earlier conjectures (e.g., Munk, 1966; Armi, 1978;

Garrett, 1990) for the importance of sloping boundary mixing, provided the above extrapolation is valid for all sloping topography. Many more future observations are needed to verify the validity of this extrapolation hypothesis, but recent ones point in the same direction.

Previous Bay of Biscay (van Haren, 2006), Hawaiian Ridge (Aucan et al., 2006; Klymak et al., 2006), Oregon continental slope (Nash et al., 2007), South China Sea (St. Laurent et al., 2011), and present (Great Meteor Seamount) data suggest that such bore-like mixing is quite universal. It seems to be independent of slope or forcing mechanism/frequency. Tides are not the only forcing mechanism for turbulence in the ocean interior, as turbulent overturns are also observed in seas that are dominated by near-inertial (e.g., Figure 1d; van Haren and Gostiaux, 2011) or subinertial (Hosegood et al., 2004) motions rather than tides. This suggests that bottom slopes do not need to critically match an internal wave slope of particular frequency for ultimate nonlinear frontal steepening. Vigorous bore-like motions and/or enhanced near-bottom turbulence have also been observed at a variety of (tidally) noncritical slopes (e.g., Klymak and Moum, 2003; Hosegood et al., 2004; van Haren, 2006; Bonnin et al., 2006; Nash et al., 2007).

Despite all the turbulent power of 50 m breaking waves above topography, very little is sensed at the surface. Therefore, in order to learn more about intrinsic interaction processes, it is mandatory to continue studying internal wave-turbulence characteristics in the ocean interior and above underwater topography. For a leap forward, development of future instrumentation should be directed to a truly four-dimensional (three-dimensional spatial plus

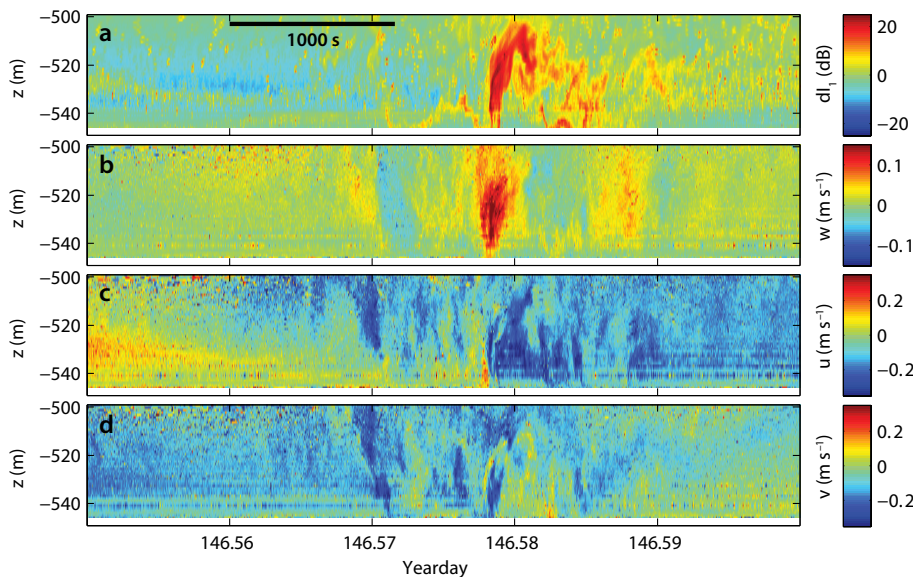



Figure 4. Time-depth images of acoustic Doppler current profiler observations from the same period as Figure 3. (a) Acoustic backscatter relative to time mean, in logarithmic dB scale (20 dB is a factor of 100 in variance change). (b) Vertical current, positive (red) is upward. (c) Cross-slope current, negative (blue) is upslope. (d) Along-slope current. All current data (panels b–d) are 30 s smoothed. Note that some depth levels show reflectance at temperature sensors.

temporal) resolution of internal wave-turbulence motions toward understanding their intrinsic properties. It should be possible to make these measurements using a multistring mooring or flotation device (Thorpe, 2010).

ACKNOWLEDGEMENTS

We thank the crews of R/V *Pelagia* and FS *Meteor* and NIOZ-MTM for deployment and recovery of moorings. We are greatly indebted to Martin Laan and Dirk-Jurjen Buijsman for continuing pleasant cooperation during the development of NIOZ temperature sensors. Construction and deployment of NIOZ temperature sensors were financed in part by investment grants (“Oceanographic equipment,” “LOCO,” “KM3NeT”) from the Netherlands organization for the advancement of scientific research (NWO) and by BSIK. We appreciate comments made by Allison Lee and Loes Gerringa on an earlier draft. 

REFERENCES

- Armi, L. 1978. Some evidence for boundary mixing in the deep ocean. *Journal of Geophysical Research* 83:1,971–1,979, <http://dx.doi.org/10.1029/JC083iC04p01971>.
- Armi, L. 1979. Effects of variations in eddy diffusivity on property distributions in the oceans. *Journal of Marine Research* 37:515–530.
- Aucan, J., M.A. Merrifield, D.S. Luther, and P. Flament. 2006. Tidal mixing events on the deep flanks of Kaena Ridge, Hawaii. *Journal of Physical Oceanography* 36:1,202–1,219, <http://dx.doi.org/10.1175/JPO2888.1>.
- Bonnin, J., H. van Haren, P. Hosegood, and G.-J.A. Brummer. 2006. Burst resuspension of seabed material at the foot of the continental slope in the Rockall Channel. *Marine Geology* 226:167–184, <http://dx.doi.org/10.1016/j.margeo.2005.11.006>.
- D’Asaro, E.A., and R.-C. Lien. 2000. The wave-turbulence transition for stratified flows. *Journal of Physical Oceanography* 30:1,669–1,678, [http://dx.doi.org/10.1175/1520-0485\(2000\)030<1669:TWTTF>2.0.CO;2](http://dx.doi.org/10.1175/1520-0485(2000)030<1669:TWTTF>2.0.CO;2).
- Dillon, T.M. 1982. Vertical overturns: A comparison of Thorpe and Ozmidov length scales. *Journal of Geophysical Research* 87:9,601–9,613, <http://dx.doi.org/10.1029/JC087iC12p09601>.
- Farmer, D.M., M.H. Alford, R.-C. Lien, Y.J. Yang, M.-H. Chang, and Q. Li. 2011. From Luzon Strait to Dongsha Plateau: Stages in the life of an internal wave. *Oceanography* 24(4):64–77, <http://dx.doi.org/10.5670/oceanog.2011.95>.
- Garrett, C. 1990. The role of secondary circulation in boundary mixing. *Journal of Geophysical Research* 95:3,181–3,188, <http://dx.doi.org/10.1029/JC095iC03p03181>.
- Garrett, C. 1991. Marginal mixing theories. *Atmosphere-Ocean* 29:313–339, <http://dx.doi.org/10.1080/07055900.1991.9649407>.
- Gerkema, T. 1996. A unified model for the generation and fission of internal tides in a rotating ocean. *Journal of Marine Research* 54:421–450, <http://dx.doi.org/10.1357/0022240963213574>.
- Gerkema, T., and H. van Haren. 2007. Internal tides and energy fluxes over Great Meteor Seamount. *Ocean Science* 3:441–449.
- Gregg, M.C. 1989. Scaling turbulent dissipation in the thermocline. *Journal of Geophysical Research* 94:9,686–9,698, <http://dx.doi.org/10.1029/JC094iC07p09686>.
- Groen, P. 1948. Contribution to the theory of internal waves. *Koninklijk Nederlands Meteorologisch Instituut Mededelingen en Verhandelingen* B11:1–23.
- Helfrich, K.R., and W.K. Melville. 2006. Long nonlinear internal waves. *Annual Review of Fluid Mechanics* 38:395–425, <http://dx.doi.org/10.1146/annurev.fluid.38.050304.092129>.
- Hosegood, P., J. Bonnin, and H. van Haren. 2004. Solibore-induced sediment resuspension in the Faeroe-Shetland Channel. *Geophysical Research Letters* 31, L09301, <http://dx.doi.org/10.1029/2004GL019544>.
- Klymak, J.M., and J.N. Moum. 2003. Internal solitary waves of elevation advancing on a shoaling shelf. *Geophysical Research Letters* 30, 2045, <http://dx.doi.org/10.1029/2003GL017706>.
- Klymak, J.M., J.N. Moum, J.D. Nash, E. Kunze, J.B. Girton, G.S. Carter, C.M. Lee, T.B. Sanford, and M.C. Gregg. 2006. An estimate of tidal energy lost to turbulence at the Hawaiian Ridge. *Journal of Physical Oceanography* 36:1,148–1,164, <http://dx.doi.org/10.1175/JPO2885.1>.
- Mohn, C., and A. Beckmann. 2002. The upper ocean circulation at Great Meteor Seamount. Part I: Structure of density and flow fields. *Ocean Dynamics* 52:179–193, <http://dx.doi.org/10.1007/s10236-002-0017-4>.
- Munk, W. 1966. Abyssal recipes. *Deep-Sea Research* 13:707–730, [http://dx.doi.org/10.1016/0011-7471\(66\)90602-4](http://dx.doi.org/10.1016/0011-7471(66)90602-4).
- Munk, W., and C. Wunsch. 1998. Abyssal recipes II: Energetics of tidal and wind mixing. *Deep-Sea Research Part I* 45:1,977–2,010, [http://dx.doi.org/10.1016/S0967-0637\(98\)00070-3](http://dx.doi.org/10.1016/S0967-0637(98)00070-3).
- Nash, J.D., M.H. Alford, E. Kunze, K. Martini, and S. Kelly. 2007. Hotspots of deep ocean mixing on the Oregon continental slope. *Geophysical Research Letters* 34, L01605, <http://dx.doi.org/10.1029/2006GL028170>.
- Orr, M.H., and P.C. Mignerey. 2003. Nonlinear internal waves in the South China Sea: Observation of the conversion of depression internal waves to elevation internal waves. *Journal of Geophysical Research* 108, 3064, <http://dx.doi.org/10.1029/2001JC001163>.
- Osborn, T.R. 1980. Estimates of the local rate of vertical diffusion from dissipation measurements. *Journal of Physical Oceanography* 10:83–89, [http://dx.doi.org/10.1175/1520-0485\(1980\)010<0083:EOTLRO>2.0.CO;2](http://dx.doi.org/10.1175/1520-0485(1980)010<0083:EOTLRO>2.0.CO;2).
- St. Laurent, L., H. Simmons, T.Y. Tang, and Y.H. Wang. 2011. Turbulent properties of internal waves in the South China Sea. *Oceanography* 24(4):78–87, <http://dx.doi.org/10.5670/oceanog.2011.96>.
- Thorpe, S.A. 1977. Turbulence and mixing in a Scottish loch. *Philosophical Transactions of the Royal Society of London A* 286:125–181, <http://dx.doi.org/10.1098/rsta.1977.0112>.
- Thorpe, S.A. 1987a. Transitional phenomena and the development of turbulence in stratified fluids: A review. *Journal of Geophysical Research* 92:5,231–5,248, <http://dx.doi.org/10.1029/JC092iC05p05231>.
- Thorpe, S.A. 1987b. Current and temperature variability on the continental slope. *Philosophical Transactions of the Royal Society of London A* 323:471–517, <http://dx.doi.org/10.1098/rsta.1987.0100>.
- Thorpe, S.A. 2010. Breaking internal waves and turbulent dissipation. *Journal of Marine Research* 68:851–880, <http://dx.doi.org/10.1357/002224010796673876>.
- van Haren, H. 2005. Details of stratification in a sloping bottom boundary layer of Great Meteor Seamount. *Geophysical Research Letters* 32, L07606, <http://dx.doi.org/10.1029/2004GL022298>.
- van Haren, H. 2006. Nonlinear motions at the internal tide source. *Geophysical Research Letters* 33, L11605, <http://dx.doi.org/10.1029/2006GL025851>.
- van Haren, H., and L. Gostiaux. 2009. High-resolution open-ocean temperature spectra. *Journal of Geophysical Research* 114, C05005, <http://dx.doi.org/10.1029/2008JC004967>.
- van Haren, H., and L. Gostiaux. 2010. A deep-ocean Kelvin-Helmholtz billow train. *Geophysical Research Letters* 37, L03605, <http://dx.doi.org/10.1029/2009GL041890>.
- van Haren, H., and L. Gostiaux. 2011. Large internal waves advection in very weakly stratified deep Mediterranean waters. *Geophysical Research Letters* 38, L22603, <http://dx.doi.org/10.1029/2011GL049707>.
- van Haren, H., and L. Gostiaux. 2012. Detailed internal wave mixing observed above a deep-ocean slope. *Journal of Marine Research* 70:173–197, <http://dx.doi.org/10.1357/002224012800502363>.
- van Haren, H., L. Gostiaux, M. Laan, M. van Haren, E. van Haren, and L.J.A. Gerringa. 2012. Internal wave turbulence near a Texel beach. *PLoS ONE* 7(3), e32535, <http://dx.doi.org/10.1371/journal.pone.0032535>.
- van Haren, H., M. Laan, D.-J. Buijsman, L. Gostiaux, M.G. Smit, and E. Keijzer. 2009. NIOZ3: Independent temperature sensors sampling yearlong data at a rate of 1 Hz. *IEEE Journal of Oceanic Engineering* 34:315–322, <http://dx.doi.org/10.1109/OJEO.2009.2021237>.
- Vlasenko, V., and K. Hutter. 2002. Numerical experiments on the breaking of solitary internal waves over a slope-shelf topography. *Journal of Physical Oceanography* 32:1,779–1,793, [http://dx.doi.org/10.1175/1520-0485\(2002\)032<1779:NEOTBO>2.0.CO;2](http://dx.doi.org/10.1175/1520-0485(2002)032<1779:NEOTBO>2.0.CO;2).